Measuring and Predicting the Dynamics of Linear Monodisperse Entangled Polymers in Rapid Flow through an Abrupt Contraction. A Small Angle Neutron Scattering Study

R. S. Graham,*,†,# J. Bent,‡ L. R. Hutchings,‡ R. W. Richards,‡,¶ D. J. Groves,† J. Embery,† T. M. Nicholson,○,† T. C. B. McLeish,† A. E. Likhtman,§ O. G. Harlen,§ D. J. Read,§ T. Gough,⊥ R. Spares,⊥ P. D. Coates,⊥ and I. Grillo||

Department of Physics and Astronomy, University of Leeds, Leeds LS2 9JT, U.K., Department of Chemistry, University of Durham, Durham DH1 3LE, U.K., Department of Applied Mathematics, University of Leeds, Leeds LS2 9JT, U.K., School of Engineering, Design and Technology, University of Bradford, Bradford BD7 1DP, U.K., Institut Laue-Langevin, 34042 Grenoble Cedex 9, France, Department of Chemical Engineering, University of Michigan, Ann Arbor, Michigan 48109, Division of Chemical Engineering, University of Queensland, St. Lucia, Queensland 4072, Australia, and EPSRC, Polaris House, North Star Avenue, Swindon SN2 1ET, U.K.

Received November 4, 2005; Revised Manuscript Received February 8, 2006

ABSTRACT: Small-angle neutron scattering measurements on a series of monodisperse linear entangled polystyrene melts in nonlinear flow through an abrupt 4:1 contraction have been made. Clear signatures of melt deformation and subsequent relaxation can be observed in the scattering patterns, which were taken along the centerline. These data are compared with the predictions of a recently derived molecular theory. Two levels of molecular theory are used: a detailed equation describing the evolution of molecular structure over all length scales relevant to the scattering data and a simplified version of the model, which is suitable for finite element computations. The velocity field for the complex melt flow is computed using the simplified model and scattering predictions are made by feeding these flow histories into the detailed model. The modeling quantitatively captures the full scattering intensity patterns over a broad range of data with independent variation of position within the contraction geometry, bulk flow rate and melt molecular weight. The study provides a strong, quantitative validation of current theoretical ideas concerning the microscopic dynamics of entangled polymers which builds upon existing comparisons with nonlinear mechanical stress data. Furthermore, we are able to confirm the appreciable length scale dependence of relaxation in polymer melts and highlight some wider implications of this phenomenon.

1. Introduction

Modern theories for the dynamics of concentrated polymer fluids are most frequently based on the tube model of DeGennes, Doi, and Edwards.[1,2] Under this approach, the complicated many-body interactions between neighboring chains, which dominate the molecular dynamics in this regime, are modeled, in a mean-field manner, as an effective tubelike constraint around a test chain. This appealingly simple approach has led to a significant number of theoretical breakthroughs. In the long-term, it offers the possibility of comprehensive ab initio predictions for a wide range of relevant macroscopic properties as a function of molecular weight distribution and branching structure of the fluid. However, the current challenge is to elucidate the essential physics by systematic comparisons with data for polymer fluids of controlled molecular weight distribution and molecular architecture.

Tube models are primarily appraised by the accuracy of their rheological predictions, and with good reason. Stress predictions are of paramount importance in practical situations since they are necessary for flow computation calculations. Stresses are also readily related to molecular structure and these measurements have been used extensively to gain molecular insight. Furthermore, rheological equipment is widely available, so data are abundant. However, the skill and ingenuity required to produce high precision rheological measurements for entangled polymers, particularly in extension, should not be underestimated.[3−7]

The tube picture is able to produce predictions on a level of detail that goes well beyond the minimum requirement for rheological measurements. The most detailed models describe the chain configuration over a range of length scales[8,9] and, in the case of linear polymers, this level of detail is necessary for quantitative ab initio rheological predictions, especially if variations with molecular weight are to be captured. Such theories make predictions over length scales ranging from the whole chain contour down to the tube diameter. In contrast, mechanical stresses depend only upon on average over all of these length scales. Furthermore, the tube concept leads to some very specific predictions for the variation of chain relaxation with length scale. For example, it predicts that the end segments of a chain will relax much faster than segments close to the chain center, as a direct consequence of chain diffusion in the tube. Consequently, since the stress is an equally weighted average over contributions from all length scales, one would expect that, after a deformation, a large portion of the mechanical stresses will relax noticeably faster than the chain end-to-end vector. Stress measurements can provide, at best, only an implicit probe to these rather specific predictions. Moreover,

* Corresponding author. E-mail: r.s.graham@leeds.ac.uk.
† Department of Physics and Astronomy, University of Leeds.
‡ Department of Chemistry, University of Durham.
§ Department of Applied Mathematics, University of Leeds.
⊥ School of Engineering, Design and Technology, University of Bradford.
|| Institut Laue-Langevin.
Department of Chemical Engineering, University of Michigan.
○ Division of Chemical Engineering, University of Queensland.
¶ EPSRC, Polaris House.

10.1021/ma052357z CCC: $33.50
Published on Web 03/11/2006

accurate predictions across all length scales are a prerequisite to the long-term aim of mapping molecular dynamics to solid-state properties via process modeling. A new generation of increasingly direct molecular probes are being employed to provide a more complete experimental picture of the dynamics of entangled polymers. Theoretical insights are also beginning to be gained by analyzing such data.[10−14] For a recent overview of these techniques and their relevance to theoretical developments see reference.[15] Since such techniques can observe the variation of relaxation with length scale, it is an extremely pertinent question to ask how closely tube based models can capture the results of these direct molecular probes.

In this paper, we use small-angle neutron scattering (SANS) measurements to study the evolution of the single chain structure factor of a series of monodisperse linear polymer melts passing rapidly through an abrupt contraction. We directly compare these SANS data, collected from a range of molecular weights and flow rates, with a detailed nonlinear molecular theory. The results highlight how the highly cooperative nature of chain relaxation in entangled polymers leads to extensive length scale dependent relaxation, as observed in both experiment and theory.

2. Small-Angle Neutron Scattering from Polymers under Flow

Experimental studies of small-angle neutron scattering (SANS) from entangled polymer melts under flow are rare even though the relevant spatial scales are ideally matched. A significant difficulty is that the time required to obtain good statistics from SANS, of the order of tens of minutes, is far longer than the time scale of nonlinear rheological response. One approach is to deform the melt and then rapidly quench it to below its glass transition temperature. The frozen chain configurations can then be probed by scattering experiments with the sample in the glassy state. This approach has been applied to both shear[16] and extensional flows.[17−19] Recent advances in deformation and temperature control have resulted in successful measurement and analysis of data from both linear[13] and branched[12] model polymers. Extreme care must be made to ensure that the quench is sufficiently rapid to ensure that the anisotropy does not relax significantly during this step, particularly the fast-relaxing shorter length scales. This can diminish the desirable ability to measure chain configuration across a range of length scales.

An alternative is to perform in situ SANS measurements on a sample under steady flow. Such experiments have the potential to be sensitive to the simultaneous action of many of the relaxation mechanisms in the tube theory. Unfortunately, the considerable challenges of combining the difficult rheological and scattering experiments in a viscometric flow geometry have yet to be met.

2.1. SANS Study of Melt Flow through a Contraction. Bent et al.[11,20] presented a novel approach to the above problems using a complex flow geometry. In these experiments monodisperse melts of deuterated polystyrene were fed through a 4:1 contraction, along a channel, then subjected to a reverse expansion at the channel exit. The melt was recirculated to preserve the deuterated material and, since the flow is steady in an Eulerian sense, SANS experiments were made along a range of points on the center line (see Figure 1). Additionally, the volumetric flow rate could be varied to investigate the effect of deformation rate on molecular structure. Although the complex geometry of the flow necessitates a finite element computation, a further benefit results from this flow geometry; while the system is in an Eulerian steady state during scattering, the Lagrangian history experienced by the fluid elements will probe the transient behavior of the melt in question. Thus, the chain configurations were probed, in detail, in a prototype industrial flow.

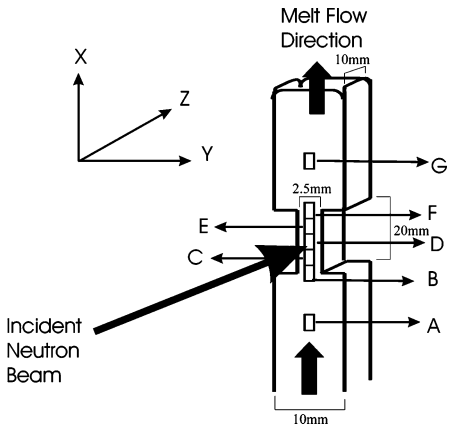

Figure 1. Diagram of the recirculation flow cell used by Bent et al., illustrating the regions of neutron sampling (slots A−G). The slot dimensions are 1 mm × 5 mm and experiments were performed at a temperature of 473K.

A preliminary comparison of these SANS data, consisting of a single molecular weight of 230 kg/mol at one deformation rate, was made with the model of Graham et al.[8] in ref 11. In this paper, we present and model a more comprehensive set of data, using a consistent parameter set, encompassing three different molecular weights, each studied at a range of deformation rates and positions along the contraction.

3. Experimental Section

3.1. Materials and Synthesis. The flow cell design, illustrated in Figure 1, and the neutron path length defined by it (∼10 mm) required that the blend of hydrogenous and deuterated polystyrene (hPS and dPS respectively) used in the SANS experiments should be composed of ∼95 wt % deuteriopolystyrene. This composition removes the high level of incoherent background that would be encountered with the classical mixture compositions, i.e., ∼10% deuteriopolymer, used in the more usual "thin" specimens with a neutron path length of ∼1 mm. Because of the long neutron path length, the high background in the more common mixtures would overwhelm the coherent scattering and hence the need to use blends of over 90% deuteriopolymer.

The total mass of polymer in the flow cell was approximately 200 g, and this mass of deuteriostyrene monomer was anionically polymerized in a 2 L stirred Buchi reaction vessel thermostated at 303 K. The reaction vessel was first evacuated and then repeatedly purged with dry nitrogen before 1 L of dry, degassed benzene was added via a special buret that prevented exposure of the solvent to air. The appropriate mass of dried and degassed deuteriostyrene was then added to the vessel from a similar buret and the mixture rapidly stirred. Polymerization was initiated by injecting the required volume (as defined by the desired polymer molecular weight) of 1.4 M sec butyllithium (Aldrich) through the septum port in the top of the reaction vessel. After 6 h, degassed methanol was injected into the living deuteriopolystyrene solution to terminate the reaction and a small sample of the resultant solution removed for determination of the molecular weight of the dPS. A known mass of hPS of essentially identical molecular weight as the dPS was added to the solution to give a hPS weight fractions of order 5%. Antioxidant Irganox 1076, was also dissolved in the polystyrene solution (∼1500 ppm) and the solution drained from the vessel directly into a well-stirred large excess of methanol that was also saturated with antioxidant. The precipitated dPS/hPS mixture was filtered off, washed and dried under vacuum at 313 K to constant weight and its composition determined by ^{1}H NMR on a solution in deuteriodichloromethane containing Pentaerythritol tetrachloride as a calibrant for determination of proton content and hence hPS weight fraction in the mixture. Hydrogenous polystyrene was synthesized

on the 20 g scale by conventional high vacuum methods of anionic polymerization. Molecular weights of all polystyrenes were obtained from size exclusion chromatography with mass viscosity and right angle light scattering detectors with THF as eluting solvent. Three different polystyrene mixtures, consisting of hydrogenated and deuterated chains with closely matched molecular weights, were produced. The resulting mixtures, labeled 100K, 250K, and 400K, had weight-averaged molecular weights of 110.3, 229.8, and 407.5 kg mol^{-1}. Each mixture had a polydispersity index $\leq$1.08. The respective weight fractions of deuterated material, as measured by proton NMR, are 93.42%, 93.47% and 94.69%. However, later we will show that quiescent scattering data suggest that the deuterated fractions are slightly larger ($\sim$95%, see section 4.3).

3.2. Rheological Characterization. To facilitate a detailed rheological characterization a further series of hPS materials was synthesized with molecular weights ranging (in g mol^{-1}) from 68k to 501k. Linear oscillatory shear and transient nonlinear shear measurements were made using a Rheometrics ARES rheometer. Full details of this study, including a comparison with molecular theory in linear and nonlinear response for both viscometric and complex flows, are given in reference.[21] Similarly, the linear rheology of dPS materials was measured and found to be consistent with this earlier study.

3.3. Recirculation Flow Cell. The design, construction, and details of the use of the recirculation flow cell (RFC) have been provided elsewhere,[20] but a summary is included here for completeness. Polystyrene melt is fed from a heated reservoir by a gear pump to a flow channel on which the neutron beam is incident and the melt is then returned to the reservoir. Before use the whole RFC was purged with dry nitrogen and then sealed to prevent entry of air and moisture. Heaters were placed at appropriate points on the complete assembly (reservoir, flow channel, return, and delivery tubing and the gear pump) and maintained the temperature at 473 K via dedicated PID temperature controllers. The flow channel on which the neutron beam was incident on the flowing polymer melt had an initially square cross section of 10×10 mm^2 and extended for 100 mm in the flow (or X) direction. At this point there was an abrupt contraction of the flow path in the Y direction to 2.5 mm, i.e., a 4:1 contraction in one dimension. This flow path of reduced cross section extended in the flow direction for 20 mm and effectively constitutes a slot die with dimensions (XYZ) of $20 \times 2.5 \times 10$ mm^3. After 20 mm in the X direction, the flow path abruptly expands to its original cross section of 10×10 mm^2 and this continues for 100 mm in the X direction where the polymer melt enters the return tube to the reservoir. A range of volumetric flow rates for each polymer melt has been explored, the magnitudes being determined by the rotational speed of the gear pump and the maximum safe working pressure of the RFC. Higher molecular weight polymers generated larger back pressures for the same volumetric flow rate. SEC analysis of all three hPS/dPS mixtures was repeated once all scattering experiments were complete. No degradation of molecular weight or increase in polydispersity was observed for any of the melts. SANS data for the 250K material at a flow rate of 0.75 cm^3/s obtained using this cell were reported in earlier publications,[20,11] together with birefringence data showing the development of stress contours in the flowing melt as it enters the slot die. In this study, we present new data for two additional molecular weights and investigate the effect of varying the volumetric flow rate. These new data are analyzed along with this previously published data from the cell.

3.4. SANS Experiments. All SANS data were collected using the D22 small angle diffractometer at the Institut Laue-Langevin, Grenoble, France. The incident neutron beam wavelength was 10 Å with a sample−detector distance set at 5.6 m. This instrument arrangement gave a scattering vector range in the vertical direction, parallel to the polymer melt flow direction of $6 \times 10^{-3} \leq Q/\text{Å}^{-1} \leq 5 \times 10^{-2}$ and in the direction perpendicular to the flow direction the accessible Q range was $5.0 \times 10^{-3} \leq Q/\text{Å}^{-1} \leq 0.1$. The RFC was mounted on a table that could be translated vertically and horizontally with respect to the incident neutron beam. A cadmium diaphragm immediately before the RFC defined the incident beam shape and dimensions, this had a rectangular cross-section with dimensions of 5×1 mm^2 and the neutron beam was incident on the center line of the polymer melt flow at the regions of finite area indicated in Figure 1. At this point we emphasize that the neutron beam cross section of 5 mm^2 is an order of magnitude smaller than that normally used ($\sim$70 mm^2) and that there was no significant variation in beam intensity across this small aperture. The scattering data collected were normalized for variations in detector response and efficiency by dividing each data set by the scattering from a 1 mm thick specimen of light water; this also placed the scattered intensity on an absolute scattering cross section scale since the scattering cross section of water is known as a function of incident neutron beam wavelength. No anisotropy was observed in the scattering patterns for the 100K material even at the highest achieved volumetric flow rate of 2.1 cm^2/s. However, significant anisotropy occurred in the scattering patterns for the 250K and 400K materials (see section 6.2).

4. Molecular Theory

4.1. Refinements of the Tube Model. The original tube model, of one-dimensional diffusion or reptation, has been extensively refined, guided mainly by evidence from rheological measurements. For linear polymers, researchers added numerous second-order effects to improve the predictions and internal consistency of the model. In linear response, the most significant of these are: contour length fluctuations (CLF),[22] thermal constraint release[23,24] and longitudinal Rouse modes.[25] Likhtman and McLeish[25] recently incorporated all of these mechanisms into a comprehensive model of the linear dynamics of linear polymers that quantitatively captures a wide range of experimental data. In the nonlinear regime one must also add the processes of chain stretch[26,27] and convective constraint release (CCR),[28] both of which are necessary to obtain even qualitative agreement with observed phenomena. Graham et al.[8] included these mechanisms in their derivation of a complementary nonlinear model to the Likhtman and McLeish theory. In their approach, all model parameters are independent of molecular weight and can be obtained from linear oscillatory shear measurements alone. Nonlinear predictions are made without modifying these, or any parameters. Despite the absence of nonlinear fitting the model accurately predicts the variation in rheological response due to changes in molecular weight, chemical composition, and deformation geometry observed in a comprehensive set of rheological data collected from several experimental groups. While this agreement with rheological data is very encouraging, comparison with SANS data presents a significantly more demanding challenge.

4.2. A Molecular Model for Strong Flows. In this section, we briefly review the model of Graham et al.[8] The model is derived from a microscopic expression for the dynamics of the space-curve describing the chain contour, $\mathbf{R}(s, t)$. The variable s labels monomers along the tube and runs from $s = 0$ to Z, where Z is the number of entanglements ($Z = N/N_e$, N is the number of monomers per chain, N_e the number of monomers per entanglement segment, and the tube diameter is a). Combining the effects of the relaxation mechanisms discussed above leads to a stochastic equation for $\mathbf{R}(s, t)$,

$$\mathbf{R}(s, t + \Delta t) = \mathbf{R}\left(s + \frac{Z}{Z^*(t)}\Delta\xi(t), t\right) + \Delta t\left[\kappa\cdot\mathbf{R} + \frac{3\nu}{2}\frac{a}{|\mathbf{R}'|}\mathbf{R}'' + \tilde{\mathbf{g}}(s, t) + \frac{1}{2\pi^2\tau_e}\left(\mathbf{R}'\frac{\partial}{\partial s}\ln(\mathbf{R}'\cdot\mathbf{R}')\right)\right]$$

where the primes denote derivatives with respect to monomer number, s. The first term represents reptation, the second

represents convection (κ is the velocity gradient tensor), the third and fourth describe constraint release leading to Rouse-like motion of the tube, and the final term is retraction of the chain along the tube, driven by the entropic spring force of the chain. The Rouse time of an entanglement segment is denoted by τ_e, and ν is the rate of constraint release which is found self-consistently by computing the instantaneous chain retraction rate from the chain configuration. The equation contains two stochastic terms, $\tilde{\mathbf{g}}(s, t)$ and $\Delta\xi(t)$, which are both mean zero Gaussian random variables with the following moments

$$\langle \Delta\xi(t)\Delta\xi(t')\rangle = \frac{2}{3\pi^2 Z\tau_e}\delta(t-t') \quad \text{and}$$

$$\langle \tilde{g}_\alpha(s,t)\,\tilde{g}_\beta(s',t')\rangle = \nu a^2 \frac{a}{|\mathbf{R}'(s)|}\Delta(s-s')\delta(t-t')\delta_{\alpha\beta}$$

From the chain configuration the stress and the single chain structure factor can be obtained from the average, $f_{\alpha\beta}(s, s') = \langle \partial R_\alpha(s)/\partial s \times \partial R_\beta(s')/\partial s'\rangle$, where α and β denote Cartesian components. A deterministic evolution equation for $\mathbf{f}(s, s')$ is derived from the above equation, using several decoupling approximations and introducing CLF in an approximate way, to give,

$$\frac{\partial \mathbf{f}}{\partial t} = \boldsymbol{\kappa}\cdot\mathbf{f} + \mathbf{f}\cdot\boldsymbol{\kappa}^T + \frac{1}{3\pi^2\tau_e}\frac{a}{\sqrt{\mathrm{Tr}\mathbf{f}(s_{\min}, s_{\min})}}\left(\frac{\partial}{\partial s}+\frac{\partial}{\partial s'}\right)\times \left(\frac{aD_{\mathrm{CLF}}(s,s')}{\sqrt{\mathrm{Tr}\mathbf{f}(s_{\min}, s_{\min})}}\left(\frac{\partial}{\partial s}+\frac{\partial}{\partial s'}\right)\mathbf{f}\right) + \frac{3\nu a}{2}\left[\frac{\partial}{\partial s}\left(\frac{a}{\sqrt{\mathrm{Tr}\mathbf{f}(s,s)}}\frac{\partial}{\partial s}(\mathbf{f}-\mathbf{f}^{\mathrm{eq}})\right) + \frac{\partial}{\partial s'}\left(\frac{a}{\sqrt{\mathrm{Tr}\mathbf{f}(s',s')}}\frac{\partial}{\partial s'}(\mathbf{f}-\mathbf{f}^{\mathrm{eq}})\right)\right] + \frac{\mathscr{R}_s}{2\pi^2\tau_e}\left[\frac{\partial}{\partial s}\left(\mathbf{f}\frac{\partial}{\partial s}\ln[\mathrm{Tr}\mathbf{f}(s,s)]\right) + \frac{\partial}{\partial s'}\left(\mathbf{f}\frac{\partial}{\partial s'}\ln[\mathrm{Tr}\mathbf{f}(s',s')]\right)\right] \quad (1)$$

Full details of the physical origin of these terms, along with the derivation of eq 1, are contained in refs 8 and 29. The parameter $\mathscr{R}_s$ accounts for the decoupling approximation used in the retraction term and Graham et al. demonstrated that a universal value of $\mathscr{R}_s = 2.0$ optimizes the agreement with experimental data for their entire data comparison. Similarly, c_ν controls the strength of constraint release and both physical arguments and rheological data indicate a value of order $c_\nu = 0.1$. We fixed these universal parameters at the above values for *all* calculations in this report, thus we use an identical approach for scattering calculations to that previously used for stress predictions.

4.3. Parameter Determination. To compute the evolution of chain structure the model requires two physical parameters: the entanglement molecular weight, M_e, and the Rouse time of an entanglement segment, τ_e. Both depend on chemistry but are independent of molecular weight and can be determined by linear rheological measurements alone. At small strains, the theory of Graham et al.[8] is in agreement with the linear theory of Likhtman and McLeish.[25] Comparison of the Likhtman and McLeish theory with oscillatory shear measurements on the dPS/hPS materials gives values of $M_e = 16.43$ kg/mol and $\tau_e = 9.66 \times 10^{-5}$ s, at 473 K.[21] Thus, the number of entanglements, $Z = M_w/M_e$, is 7, 14, and 25 for the 100K, 250K, and 400K dPS materials, respectively. For reference, the values of the chain Rouse time are 0.005 s, 0.02 s and 0.06 s for the 100K, 250K, and 400K materials, respectively, following from the relationship $\tau_R = Z^2\tau_e$. Similarly, the reptation time, τ_d, corrected for contour length fluctuations, is calculated from the series,[25]

$$\tau_d = 3Z^3\tau_e\left(1 - \frac{2.38}{Z^{1/2}} + \frac{4.17}{Z} - \frac{1.55}{Z^{3/2}}\right) \quad (2)$$

To compare theoretical predictions with scattering data, further physical quantities, which characterize the melt scattering, are required. However, these can be obtained unambiguously from quiescent scattering data. Quiescent scattering from a mixture of amorphous, flexible polymer chains with matched degrees of polymerization, N, can be described by the following function[30]

$$\frac{\partial\Sigma}{\partial\Omega} = \frac{(b_H - b_D)^2}{V}\left(\frac{1}{N\phi_D(1-\phi_D)g_D(R_g, q)} - 2\chi\right)^{-1} + B \quad (3)$$

where R_g is the chain radius of gyration ($R_g^2 = CM_w$), ϕ_D is the weight fraction of dPS, B is the background scattering, and $g_D(R_g, q)$ is the Debye function,

$$g_D(R_g, q) = \frac{2}{(q^2R_g^2)^2}(q^2R_g^2 + \exp(-q^2R_g^2) - 1) \quad (4)$$

The parameter χ denotes the segment−segment interaction between hPS and dPS monomers, which accounts for nonideal mixing of the hPS/dPS materials and is expected to be positive and small. Later we will show that the effect of χ on our data is negligible. For now we set $\chi = 0$. From ref 31 comes the hPS monomer scattering length, $b_H = 2.328 \times 10^{-12}$cm, the dPS monomer scattering length, $b_D = 10.656 \times 10^{-12}$cm, and the monomer volume, $V = 165 \times 10^{-24}$cm^3. In principle, the incoherent scattering contribution to the background, B, can be predicted from known incoherent cross sections. However, we expect additional contributions to the background scattering and so we take B is be a constant across all molecular weights, to be found by fitting eq 3 to quiescent data.

The constants C and B are independent of M_w and ϕ_D, and they were determined by simultaneously fitting the quiescent scattering data for all three materials, using the values of M_w and ϕ_D obtained in section 3.1. To optimize the agreement for the quiescent data, the following small shifts in fraction of dPS, relative to the values determined by NMR, were required:

$$\phi_D^{100K}\ 93.42\% \rightarrow 95.4\%$$

$$\phi_D^{250K}\ 93.47\% \rightarrow 95.8\%$$

$$\phi_D^{400K}\ 94.69\% \rightarrow 96.4\%$$

which are within the experimental uncertainties in the values determined by NMR. We emphasize that these shifts provide only an absolute scale for the scattering and do not affect the shape of the predicted scattering patterns. The fitting procedure yields values of $C = 62.3$ Å^2 (kg/mol)$^{-1}$ and $B = 0.26$ cm^{-1} (see Figure 2 for this fitting comparison). The value for the radius of gyration scale is consistent with those typically obtained for quiescent scattering from comparable dPS/hPS mixtures (see, for example, ref 32). The tube diameter, a, which is also independent of molecular weight, is found by computing the end-to-end vector of a chain of mass M_e (i.e., $a^2 = 6CM_e$) to give a value of $a = 78.3$ Å. This is equivalent to assuming that, in equilibrium, the tube is a Gaussian random walk comprising Z steps of length a. A summary of the results of

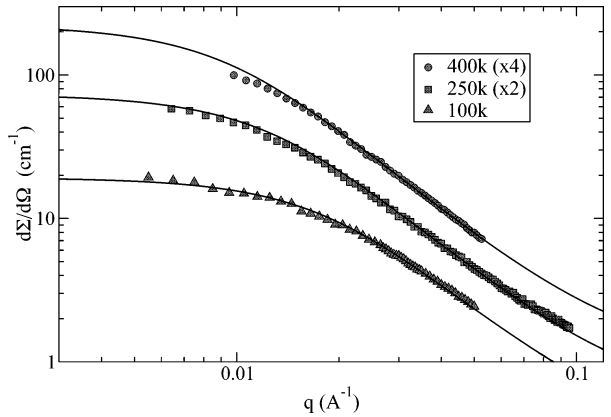

Figure 2. Quiescent data for each of the molecular weights in the study. The theory lines are simultaneous fits of eq 3. For clarity, the 250K and 400K sets have been multiplied by 2 and 4, respectively.

this characterization of the hPS/dPS mixtures is contained in Table 1, and we use these values throughout the rest of this work.

We now consider the effect of nonzero values of χ in eq 3. The effect on the calculations in Figure 2 of increasing χ from zero to values in the region $\chi \lesssim 3.0 \times 10^{-4}$ is negligible. Furthermore, reference[33] reports a value of $\chi \approx 1.7 \times 10^{-4}$ for hPS/dPS mixtures at 160 °C and this value is expected to be lower at our experimental temperature of 200 °C. Therefore, we conclude that nonideal mixing of the hPS/dPS blend makes no contribution to our scattering data.

5. Flow Visualization

Although the detailed treatment of eq 1 is required to compute scattering patterns, it is unfeasible, with present computing power, to use this model for a finite element flow computation. Such a computation is required to evaluate the fluid behavior in the contraction flow used for the SANS experiments. Fortunately, calculation of the flow field requires only a simpler constitutive equation capable of computing the stress tensor, σ. This computed flow field can be used to provide the deformation history for all streamlines passing through all regions sampled by neutron scattering. Recently, it was demonstrated that the full molecular treatment outlined above may be mapped onto a simple constitutive equation known as the Rouse−linear-entangled-polymer (Rolie-Poly) equation, which has the form[34]

$$\frac{\partial \boldsymbol{\sigma}}{\partial t} = \boldsymbol{\kappa}\cdot\boldsymbol{\sigma} + \boldsymbol{\sigma}\cdot\boldsymbol{\kappa}^{\mathrm{T}} - \frac{1}{\tau_{\mathrm{d}}}(\boldsymbol{\sigma} - \boldsymbol{I}) - \frac{2\left(1 - \sqrt{\frac{3}{\mathrm{Tr}\boldsymbol{\sigma}}}\right)}{\tau_{\mathrm{R}}}\left(\boldsymbol{\sigma} + \beta\sqrt{\frac{3}{\mathrm{Tr}\,\boldsymbol{\sigma}}}(\boldsymbol{\sigma} - \boldsymbol{I})\right) \quad (5)$$

Following the approach of Likhtman and Graham[34] we fitted a five-mode Rolie-Poly model to both experimental shear data and the predictions of the detailed model in both linear and nonlinear response. The flow and stress fields for this constitutive model were computed using our in-house Lagrangian viscoelastic code, FlowSolve.[35,36] To confirm the reliability of these calculations, stress predictions were compared to experimental birefringence data. Figure 3 shows the close agreement between data and theory, demonstrating that the Rolie-Poly model accurately captures the stress. The velocity profiles along streamlines that enter the neutron beam were computed for use in the full model. Fluid elements passing along the center line experience a variable rate planar extensional flow since, by symmetry, there is no shear along this line and there is no flow parallel to the neutron beam. Velocity gradient calculations of streamlines passing along the edges of the neutron sampling region find almost exactly the flow field as those on the center line, indicating that the material is in plug-flow. All shear is concentrated close to the contraction wall and so the deformation experienced by fluid elements passing through the neutron beam is dominated by planar extension. As Figure 3 shows, the fluid experiences a burst of extension just before the contraction entrance and a slightly weaker reverse flow at the contraction exit. The numerical procedure was repeated to provide velocity gradient histories for the 400K material. When plotted in the following reduced form: $t\dot{V}$, $\dot{\epsilon}/\dot{V}$, where $\dot{V}$ is the bulk volumetric flow rate, the velocity gradient data all collapse to a single curve, even across the different molecular weights. This indicates that the velocity gradient history along all streamlines passing through the neutron beam is dominated by the bulk flow kinematics and is not strongly sensitive to the constitutive behavior of the melt. In contrast, the chain configuration resulting from these velocity gradients will depend strongly on flow rate and molecular weight.

Our flowSolve calculations show that, for any given volumetric flow rate, the peak extension rate can be estimated as $\dot{\epsilon} \approx 13.3\ \mathrm{cm}^{-3}\,\dot{V}$, which allows us to calculate flow Weissenberg numbers with respect to the chain relaxation times. Table 2 summarizes the maximum achieved flow regimes for each material in the study. In each case accumulated Hencky strains are approximately 1.5. Thus, little or no deformation is expected in the 100K material, whereas the 250K and 400K materials are in the regime $1/\tau_{\mathrm{d}} < \dot{\epsilon} \lesssim 1/\tau_{\mathrm{R}}$ so the deformation is sufficiently large and rapid to result in considerable anisotropy in chain orientation, while we would expect chain stretching to be modest. Furthermore, the values of $\dot{\epsilon}\tau_{\mathrm{d}}$ for the 250K and 400K materials are very similar, and so we anticipate comparable anisotropy in the resulting scattering patterns.

6. Scattering Data and Calculation

In this section, we use the chain configurations, computed from eq 1, to produce predictions for our scattering data.

6.1. Crossover to Subtube Diameter Length Scales. The full theory outlined above predicts the shape of the coarse-grained tube path. However, it contains no details of length scales shorter than the tube, since, on these length scales, the chain is assumed to be close to an equilibrium configuration. To make scattering predictions at higher scattering vectors an appropriate crossover function is needed to describe the chain configuration on length scales smaller than the tube. We achieve this by assuming that the chains have Gaussian statistics on these shorter length scales in a similar approach to that applied to the Warner−Edwards model[37] for chain localization due to entanglements in polymer networks.[38] This derivation is shown in appendix A and it leads to the following expression for the single chain structure factor in terms of the deformed tube path, $\mathbf{f}(s, s')$

$$S(\boldsymbol{q}) = \frac{A}{Z^2}\int_0^Z \int_0^Z \exp\left(-\sum_{\alpha,\beta}\frac{a^2 q_\alpha q_\beta}{2}\left[\int_s^{s'}\int_s^{s'}(f_{\alpha\beta}(s_1, s_2) - f^{\mathrm{eq}}_{\alpha\beta}(s_1, s_2))\,\mathrm{d}s_1\,\mathrm{d}s_2 + \frac{\delta_{\alpha\beta}}{3}\left|s - s'\right|\right]\right)\mathrm{d}s\,\mathrm{d}s' + B \quad (6)$$

where A is the contrast factor $A = (b_{\mathrm{H}} - b_{\mathrm{D}})^2 N\phi_{\mathrm{D}}(1 - \phi_{\mathrm{D}})/V$. Thus, the evolution of $\mathbf{f}(s, s')$ is computed via eq 1 and from this the scattering predictions can be obtained from eq 6. This

Table 1. Summary of HPS/DPS Series Characterization

Molecular Weight Independent Values

parameter	definition	value	obtained by
τ_e	Rouse time of an entanglement segment	9.66×10^{-5} s	fitting Likhtman and McLeish
M_e	entanglement mol wt	16.43 kg/mol	model to linear rheology
B	incoherent scattering	0.26 cm^{-1}	fitting eq 3 to quiescent
C	radius of gyration scale	62.3 $Å^2$ $(kg/mol)^{-1}$	scattering data
a	tube diameter	78.3 Å	$a^2 = 6CM_e$

Molecular Weight Dependent Values

parameter	definition	100K	250K	400K	obtained by
M_w	mol wt (kg mol^{-1})	110	230	407	SEC
ϕ_D	wt % concn of dPS	95.4	95.8	96.4	NMR[a]
R_g	radius of gyration (Å)	83	120	159	$R_g^2 = CM_w$
Z	no. of entanglements	7	14	25	$Z = M_w/M_e$
τ_R	chain Rouse time (s)	0.005	0.02	0.06	$\tau_R = Z^2\tau_e$
τ_d	chain reptation time (s)	0.02	0.29	2.1	eq 2

[a]A small shift was applied to these values to optimize the agreement with quiescent data.

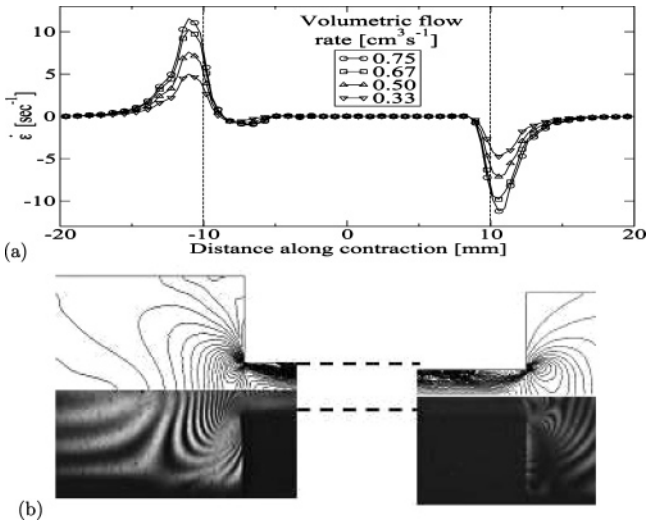

Figure 3. Flow visualization of the contraction flow for PS 250K: (a) Variation of planar extension rate along the contraction center line as computed for a range of flow rates. (b) Experimental and predicted contours of principal stress difference for a flow rate corresponding closely to the maximum rate in the SANS experiment. Part b reprinted with permission from ref 11. Copyright 2003 AAAS.

Table 2. Summary of Maximum Achieved Flow Regimes for Each Molecular Weight Using Time Scales Calculated in Table 1

M_w	max volumetric flow rate (cm^3/s)	max $\dot{\epsilon}$ (s^{-1})	$\dot{\epsilon}\tau_d$	$\dot{\epsilon}\tau_R$
100K	2.1	28.0	0.5	0.12
250K	0.75	13.3	2.9	0.19
400K	0.1	1.22	2.7	0.08

equation is the analogue of eq 3 for deformed polymers, with $\chi = 0$, and it collapses to this Debye function in the quiescent limit, as required.

6.2. Contour Plot Comparison. The dimensions of the neutron beam dictates that the scattering data could not be regarded as originating from a single point (the slot dimensions are 5 mm × 1 mm and see Figure 1 for cell dimensions). As shown above, there is no significant variation across the width of the neutron sampling area. However, chain conformation will vary along the length of the neutron beam. To account for the finite length of the scattering region, each slot was divided into equally spaced points along the center-line. The velocity gradient tensor, $\kappa(t)$, along the center-line was used to compute the chain configuration tensor, $\mathbf{f}(s, s')$, at each point, by numerical solution of eq 1, with the molecular parameters identified in section 4.3. The resulting scattering intensity from the whole slot was then computed by averaging the computed scattering intensity from each point. The number of points was increased until scattering calculations were insensitive to this value. These calculations were performed for all slots, at each available flow rate, for the three PS melts in the study. Selected data comparisons are shown in Figure 4, where the anisotropy at a range of positions along the contraction is compared at fixed flow rate. Figure 5 shows the effect of flow rate on chain configuration in the contraction entrance, the region of greatest deformation. A similar degree of agreement between data and theory was obtained for the remaining data in the study. As discussed above, no anisotropy was observed in any of the data from the 100K material, including the maximum achieved flow rate of 2.1 cm^3/s. The theory correctly predicts the absence of molecular deformation in this flow regime for the 100K material. No deformation occurs in the 100K material since the local velocity gradients produced at the measured flow rates never exceed the inverse of the longest relaxation time of the melt (see Table 2).

The majority of features of this rich data set are captured quantitatively by the model. For the 250K material, the model accurately predicts the strong chain anisotropy across a range of length scales at the contraction entrance, followed by the variation of relaxation rate with length scale as the melt moves through the narrow channel. The decay length of the SANS data along the contraction is correctly predicted for both molecular weights. Of particular note is the reversed anisotropy in the data, occurring at the contraction exit (slot F), which is correctly predicted by the model. This reversed anisotropy is due to the compression that the melt experiences as it exits the narrow channel.

Although overall agreement is good, direct comparison of the theoretical and experimental isointensity curves of Figure 5 at the lower scattering vector range shows that the small discrepancies grow with both molecular weight and deformation rate, especially in the direction perpendicular to the extension. Experimentally the chains contract less in this direction than theory predicts, even including the effect of CCR, which is a strong equilibrator of chain structure. This overprediction of the deformation may indicate that SANS measurements are sensitive to a relaxation process to which stress measurements are not. A strong candidate is tube deformation[39] in which the tube potential is deformed by the flow. A molecular weight dependence may be anticipated since the degree of tube deformation will depend on the molecular deformation on length scales approaching the tube diameter, which, in turn, would depend on molecular weight. However, further experimental data

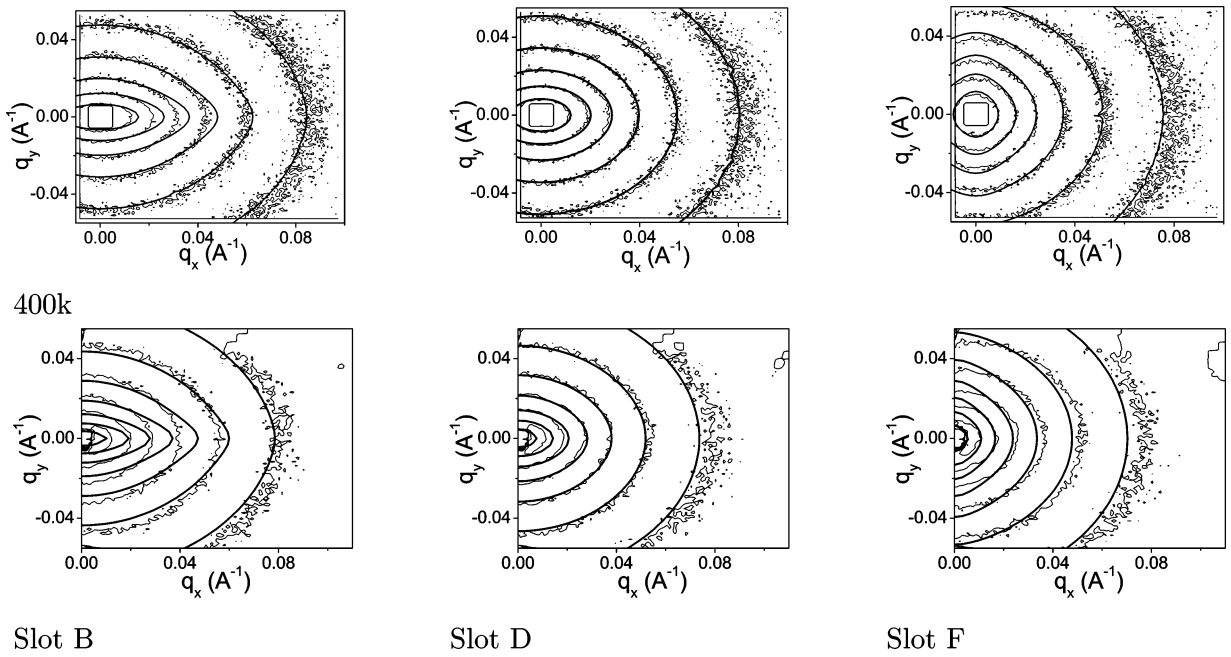

Figure 4. Scattering data and theory for 250K and 400K at 0.75 and 0.1 $cm^3\ s^{-1}$, respectively, at a range of points along the contraction. The isointensity curves correspond to values of 22, 12, 6.6, 3.6, 2.0, 1.1, and 0.6 cm^{-1}. See Figure 1 for the slot positions. 250K data and modeling reprinted with permission from ref 11. Copyright 2003 AAAS.

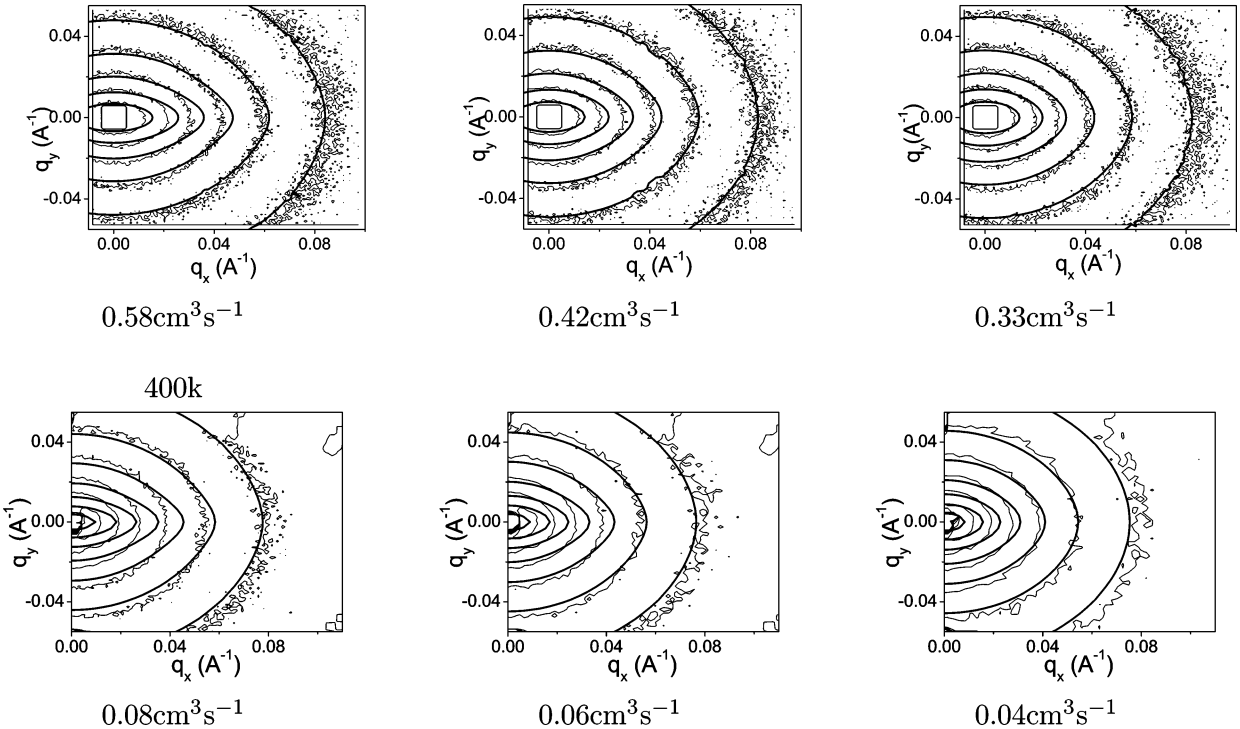

Figure 5. Scattering data and theory at slot B for a range of bulk flow rates. The isointensity curves correspond to values of 22, 12, 6.6, 3.6, 2.0, 1.1, and 0.6 cm^{-1}.

and theoretical work are needed to confirm if this overprediction, particularly with larger molecular weights, is systematic.

6.3. Comparison of Radius of Gyration and Birefringence Decay Lengths. It would be desirable to obtain a single number characterizing the degree of deformation as measured by the SANS experiments to produce a concise analysis of this extensive data set. Bent et al. fitted a Debye function to 30° sections of their deformed data to obtain an effective radius of gyration in the directions parallel and perpendicular to the flow. However the use of the Debye function in this process is a little ambiguous since the degree of chain deformation varies with length scale. Instead we wish to focus on the deformation on the length scale of the chain end-to-end vector, to which the lowest q region of the scattering data corresponds. Ideally one would like to use a Guinier relation such as

$$R_g^2 = 3 \lim_{q \to 0} \frac{\ln[S_0/S(q)]}{q^2} \tag{7}$$

to obtain the deformed radius of gyration in the limit of zero scattering vector. However, the data in this study do not reach low enough scattering angles to clearly define this limiting value,

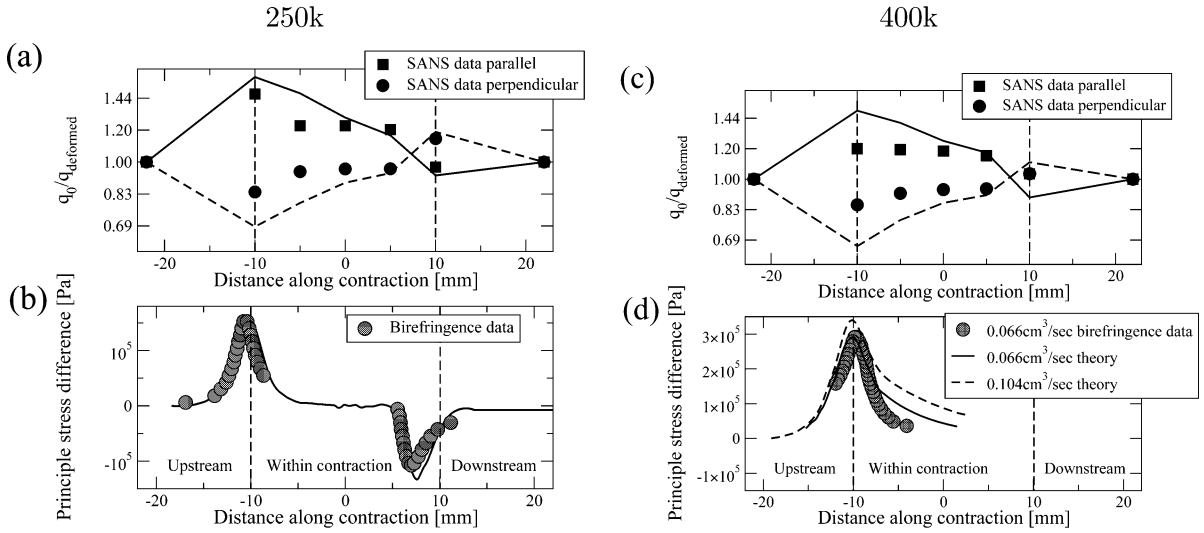

Figure 6. Comparison of chain anisotropy on the whole chain length scale as measured by SANS ($q_0/q_{deformed}$) and birefringence (stress difference) for the 250K dPS material at a flow rate of 0.75 cm^3/s (a, b) and the 400K dPS material at a flow rate of 0.1 cm^3/s (c, d). Shapes are experimental data and lines are theoretical predictions. Part b reprinted with permission from ref 11. Copyright 2003 AAAS.

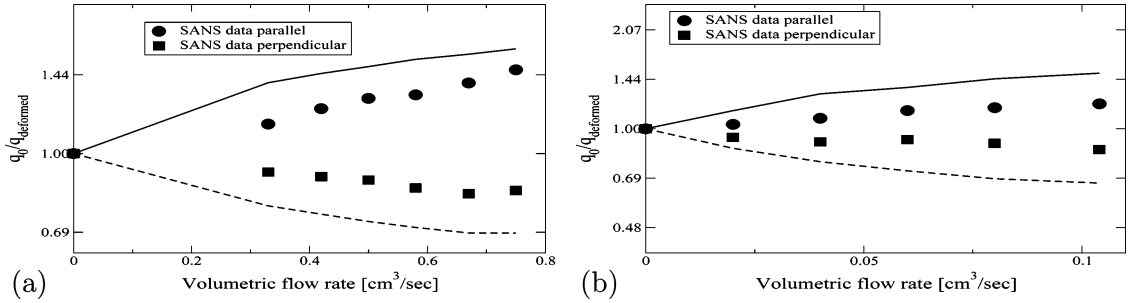

Figure 7. Chain anisotropy on the whole chain length scale at the contraction mouth (slot B) as measured by SANS for the 250K dPS (a) and 400K dPS (b) materials. Predictions for these quantities are also shown.

partially because the data exhibit increased noise for scattering vectors close to the beam stop. Nevertheless, the deformation on the length scale of the whole chain is most accurately expressed by the low q measurements and thus we focus our analysis on this region, attempting to utilize the lowest q range data that are clear of the beam stop. The degree of deformation is characterized by deviation of the isointensity curves from the circular shape of quiescent scattering (see Figures 4 and 5). To quantify this deviation we fitted ellipses to a suitably chosen isointensity curve corresponding to low q scattering. These ellipses define the experimental values of the scattering vector, at the chosen scattering intensity, in all directions. The ratio of the scattering vector from the deformed data, $q_{deformed}$, to that from quiescent data, q_0, characterizes the degree of deformation on this length scale and we examine directions parallel and perpendicular to the flow. We choose intensity values of 22 and 12 cm^{-1} for the 250K and 400K materials, respectively. In both cases, these correspond to the innermost isointensity curve in Figures 4 and 5. Furthermore, we confirmed that the ratio of principal axes of the fitted ellipses were not sensitive to the chosen intensity value in the low q range, implying that the data are approaching the limiting case of eq 7. This procedure was repeated for the theoretical predictions to produce the comparison in Figure 6 which shows the evolution of chain anisotropy through the contraction at the highest flow rate for each material.

To provide a comparison of relaxation on different length scales the decay of the principal stress difference, as measured by birefringence, is also plotted in Figure 6, along with theoretical predictions from our model. For the 400K material the highest rate for which birefringence data could be measured was a volumetric flow rate of 0.066 cm^3/s. Theoretical predictions for this rate and 0.1 cm^3/s, which corresponds to the SANS data in Figure 6c, are plotted for reference. Comparison of the SANS and birefringence data indicates that the decay length of the whole chain, within the contraction, is significantly longer than that of the birefringence as predicted by the model. This demonstrates that anisotropy can exist on the length scale of the whole chain without being detectable by birefringence. If the sample were quenched with this orientation frozen in, we would expect this effect to have implications for the solid-state properties of the material. In particular, it is feasible that solid properties could be anisotropic in a material with zero birefringence. Comparison of Figure 6a and Figure 6c shows that the relative degrees of anisotropy observed for the 250K and 400K materials are almost identical. This is expected since the flow Weissenberg number ($\dot{\epsilon}\tau_d$) is very similar for these two flows (see Table 2).

In Figure 7, the above analysis is repeated for varying flow rates, observed at the entrance to the contraction (slot B). This method of presenting the data and theory accentuates the model's overprediction of the deformation at the mouth of the contraction.

7. Conclusions

We used SANS to measure the deformation and subsequent relaxation of entangled polymer chains passing through an abrupt contraction. Our quantitative comparisons of the model of Graham et al. with this comprehensive data set indicates that this model effectively captures the results of this direct probe

of the effect of flow at the *molecular level*. In many instances the model predicts quantitatively the variation of chain relaxation over length scales ranging from the molecules as a whole, down to the tube diameter, as measured by simultaneous SANS and birefringence. The change in chain anisotropy with flow rate, molecular weight, and position along the contraction are well-described by the model, using used model parameters that are identical to those used in previous rheology-only comparisons. There is some slight, but apparently systematic, overprediction of anisotropy in the most deformed cases, particularly for the largest molecular weight. Our approach builds upon existing comparisons with mechanical stress data and the model predicts nonlinear scattering patterns from a knowledge of only the linear rheology and the quiescent scattering data of the material in question. This systematic comparison constitutes a strong confirmation of current theoretical ideas about the microscopic dynamics of entangled polymers under strong flow, at least for the range of deformation rates studied ($1/\tau_d < \dot{\epsilon} \lesssim 1/\tau_R$). Both experiment and theory elucidate the markedly different relaxation rates across the range of length scales and this phenomenon may have implications for polymer crystallization and solid-phase properties produced after quenching. The ability of the model to describe the transient chain dynamics over a wide range of length scales is essential to the modeling of these data. The regions where the model mildly overpredicts the degree of anisotropy may indicate that additional relaxation process are important in these circumstances, which suggests scope for future developments of the theory of entangled melts under strong flow.

The experimental technique and complementary analysis offer some intriguing possibilities for future studies. It is possible to perform similar measurements on other regions of the flow, for example, the rotating vortices that are observed in some contraction flows. The technique could also provide a microscopic probe of more complicated melt structures such as blends and branched architectures under flow and would be extremely useful in the development of theories for such systems. It is hoped that these comparisons with SANS data for linear polymers under nonlinear flow will motivate further progress in this fertile area.

Acknowledgment. We are grateful to the EPSRC for financial support through the Microscale Polymer Processing (μPP) grants, μPP1 (GR/M597474/01) and μPP2 (GR/T11807/01), as well as BASF, BP Chemicals, Innovene, Dow Chemical, DSM, Du Pont Teijin, and Lucite International for additional sponsorship and guidance, and to S. T. Milner and A. J. Ryan for fruitful discussions.

Appendix A. Crossover to Subtube Diameter Length Scales

The theory outlined in section 4 predicts the shape of the coarse-grained tube path but provides no detail on length scales shorter than the tube diameter, which is necessary for a data comparison across the measured range of wavevectors. In particular, the high-q scattering is dominated by chain fluctuations about the mean path defined by the tube, for which we need a suitable crossover formula. We begin with eq 5.31 from ref 40, which describes the scattering from an ideal mixture of hydrogenated and deuterated polymers with matched degrees of polymerization

$$\frac{\partial \Sigma}{\partial \Omega} = \frac{(b_H - b_D)^2}{V} N \phi_D (1 - \phi_D) P(\mathbf{q}) + B \tag{8}$$

where $P(\mathbf{q})$ is the normalized intrachain structure factor, which in our continuous notation is given by

$$P(\mathbf{q}) = \frac{1}{Z^2} \int_0^Z \int_0^Z \langle \exp(-i \sum_\alpha q_\alpha (r_\alpha(s) - r_\alpha(s'))) \rangle \, ds' \, ds \tag{9}$$

where $\mathbf{r}(s)$ denotes the position of the monomer at a distance s along the chain ($s = 0...Z$). With the separation $\mathbf{r}(s) - \mathbf{r}(s')$ taken to be a Gaussian random variable, this can be written as

$$P(\mathbf{q}) = \frac{1}{Z^2} \int_0^Z \int_0^Z \exp\left(- \sum_{\alpha\beta} \frac{q_\alpha q_\beta}{2} \langle (r_\alpha(s') - r_\alpha(s))(r_\beta(s') - r_\beta(s)) \rangle \right) ds' \, ds \tag{10}$$

Thus, we see that to compute the single chain structure factor we require an expression for the following average of the *monomer* positions, $\mathbf{r}$

$$\langle (r_\alpha(s') - r_\alpha(s))(r_\beta(s') - r_\beta(s)) \rangle \tag{11}$$

which must be valid for all length scales probed by the scattering experiment. The mean position of each monomer, $\mathbf{R}$, is defined by the tube and we assume that the statistics of $\mathbf{R}$ are given by the tube theory outlined in section 4. We denote fluctuations about this mean as $\Delta(s)$, so that

$$r_\alpha(s) = R_\alpha(s) + \Delta_\alpha(s) \tag{12}$$

Within the Warner−Edwards model, which uses quadratic localizing potentials to mimic the tube confinement, it has been shown[41] that monomer fluctuations, Δ, are not affected by deformation of the mean positions. By analogy, we assume this property in the present calculation. Defining $\overline{(...)}$ as an average over monomer fluctuations and $\langle ... \rangle$ as an average over mean positions allows us to write

$$\overline{\langle (r_\alpha(s') - r_\alpha(s))(r_\beta(s') - r_\beta(s)) \rangle} = \langle (R_\alpha(s') - R_\alpha(s))(R_\beta(s') - R_\beta(s)) \rangle + \overline{(\Delta_\alpha(s') - \Delta_\alpha(s))(\Delta_\beta(s') - \Delta_\beta(s))} \tag{13}$$

The average over mean positions can be found by integrating the deformed tube tangent correlation function as computed by the model in the previous sections

$$\langle (R_\alpha(s') - R_\alpha(s))(R_\beta(s') - R_\beta(s)) \rangle = \int_s^{s'} \int_s^{s'} f_{\alpha\beta}(s_1, s_2) \, ds_1 \, ds_2 \tag{14}$$

We may find an expression for the monomer fluctuations by insisting that eq 13 obeys the usual Gaussian statistics in equilibrium. Since the monomer fluctuations are independent of the tube deformation, the resulting expression will be valid for the deformed case as well. Thus

$$\overline{(\Delta_\alpha(s') - \Delta_\alpha(s))(\Delta_\beta(s') - \Delta_\beta(s))} = \frac{a^2 \delta_{\alpha\beta}}{3} |s - s'| - \int_s^{s'} \int_s^{s'} f_{\alpha\beta}^{eq}(s_1, s_2) \, ds_1 \, ds_2 \tag{15}$$

By substituting eqs 14 and 15 into eq 11, we obtain an expression for the average monomer positions

$$\langle (r_\alpha(s') - r_\alpha(s))(r_\beta(s') - r_\beta(s)) \rangle = \frac{a^2 \delta_{\alpha\beta}}{3} |s - s'| + \int_s^{s'} \int_s^{s'} (f_{\alpha\beta}(s_1, s_2) - f_{\alpha\beta}^{eq}(s_1, s_2)) \, ds_1 \, ds_2 \quad (16)$$

Substituting this expression into eqs 8 and 10 gives our deformed scattering expression, eq 6. If $\mathbf{f}(s, s')$ is set to its equilibrium value, we recover the quiescent expression (eq 3), with $\chi = 0$.

References and Notes

(1) de Gennes, P.-G. *J. Chem. Phys.* **1971**, *55*, 572.
(2) Doi, M.; Edwards, S. F. *The Theory of Polymer Dynamics*; Oxford University Press: Oxford, U.K., 1986.
(3) Meissner, J. *J. Appl. Polym. Sci.* **1972**, *16*, 2877.
(4) Menezes, E. V.; Graessley, W. W. *J. Polym. Sci., Part B: Polym. Phys.* **1982**, *20*, 1817.
(5) Meissner, J.; Hostettler, J. *Rheol. Acta* **1994**, *33*, 1.
(6) Münstedt, H. *J. Rheol.* **1979**, *23*, 421.
(7) Sanchez-Reyes, J.; Archer, L. A. *J. Rheol.* **2002**, *46*, 1239.
(8) Graham, R. S.; Likhtman, A. E.; McLeish, T. C. B.; Milner, S. T. *J. Rheol.* **2003**, *47*, 1171.
(9) Masubuchi, Y.; Takimoto, J. I.; Koyama, K.; Ianniruberto, G.; Marrucci, G.; Greco, F. *J. Chem. Phys.* **2001**, *115*, 4387.
(10) Wischnewski, A.; Monkenbusch, M.; Willner, L.; Richter, D.; Likhtman, A. E.; McLeish, T. C. B.; Farago, B. *Phys. Rev. Lett.* **2002**, *88*, 058301.
(11) Bent, J.; Hutchings, L. R.; Richards, R. W.; Gough, T.; Spares, R.; Coates, P. D.; Grillo, I.; Harlen, O. G.; Read, D. J.; Graham, R. S.; Likhtman, A. E.; Groves, D. J.; Nicholson, T. M.; McLeish, T. C. B. *Science* **2003**, *301*, 1691.
(12) Heinrich, M.; Pyckhout-Hintzen, W.; Allgaier, J.; Richter, D.; Straube, E.; McLeish, T. C. B.; Wiedenmann, A.; Blackwell, R. J.; Read, D. J. *Macromolecules* **2004**, *37*, 5054.
(13) Blanchard, A.; Graham, R. S.; Heinrich, M.; Pyckhout-Hintzen, W.; Richter, D.; Likhtman, A. E.; McLeish, T. C. B.;; Read, D. J.; Straube, E.; Kohlbrecher, J. *Phys. Rev. Lett.* **2005**, *95*, 166001.
(14) Likhtman, A. E. *Macromolecules* **2005**, *38*, 6128.
(15) McLeish, T. C. B. *Adv. Phys.* **2002**, *51*, 1379.
(16) Müller, R. C.; Pesce, J. J.; Picot, C. *Macromolecules* **1993**, *26*, 4356.
(17) Boué, F. *Adv. Polym. Sci.* **1987**, *82*, 47.
(18) Boué, F.; Nierlich, M.; Osaki, K. *Faraday Symp. Chem. Soc.* **1983**, *18*, 83.
(19) Mortensen, K.; Kramer, O.; Batsberg, W.; Fetters, L. *Mater. Res. Soc. Symp. Proc.* **1987**, *79*, 259.
(20) Bent, J. F.; Richards, R. W.; Gough, T. D. *Rev. Sci. Instrum.* **2003**, *74*, 4052.
(21) Collis, M. W.; Lele, A. K.; Mackley, M. R.; Graham, R. S.; Groves, D. J.; Likhtman, A. E.; Nicholson, T. M.; Harlen, O. G.; McLeish, T. C. B.; Hutchings, L. R.; Fernyhough, C. M.; Young, R. N. *J. Rheol.* **2005**, *49*, 501.
(22) Doi, M. *J. Polym. Sci., Part C: Polym. Lett.* **1981**, *19*, 265.
(23) de Gennes, P.-G. *J. Phys. (Paris)* **1975**, *36*, 1199.
(24) Rubinstein, M.; Colby, R. H. *J. Chem. Phys.* **1988**, *89*, 5291.
(25) Likhtman, A. E.; McLeish, T. C. B. *Macromolecules* **2002**, *35*, 6332.
(26) Marrucci, G.; Grizzuti, N. *Gazz. Chim. Ital.* **1988**, *118*, 179.
(27) Pearson, D.; Herbolzheimer, E.; Grizzuti, N.; Marrucci, G. *J. Polym. Sci. Part B: Polym. Phys.* **1991**, *29*, 1589.
(28) Marrucci, G. *J. Non-Newtonian Fluid Mech.* **1996**, *62*, 279.
(29) Graham, R. S. Molecular modelling of entangled polymer fluids under flow. Ph.D. Thesis, University of Leeds, 2002.
(30) de Gennes, P.-G. *Scaling Concepts in Polymer Physics*; Cornell University Press: Ithaca, NY, 1979.
(31) Wignall, G. D.; Melnichenko, Y. B. *Rep. Prog. Phys.* **2005**, *68*, 1761.
(32) Cotton, J. P.; Decker, D.; Benoit, H.; Farnoux, B.; Higgins, J.; Jannink, G.; Ober, R.; Picot, C.; des Cloizeaux, J. *Macromolecules* **1974**, *7*, 863.
(33) Bates, F. S.; Wignall, G. D. *Macromolecules* **1986**, *19*, 932.
(34) Likhtman, A. E.; Graham, R. S. *J. Non-Newtonian Fluid Mech.* **2003**, *114*, 1.
(35) Bishko, G. B.; Harlen, O. G.; McLeish, T. C. B.; Nicholson, T. M. *J. Non-Newtonian Fluid Mech.* **1999**, *82*, 255.
(36) Lee, K.; Mackley, M. R.; McLeish, T. C. B.; Nicholson, T. M.; Harlen, O. G. *J. Rheol.* **2001**, *45*, 1261.
(37) Warner, M.; Edwards, S. F. *J. Phys. A: Math. Gen.* **1978**, *11*, 1649.
(38) Read, D. J.; McLeish, T. C. B. *Macromolecules* **1997**, *30*, 6376.
(39) Rubinstein, M.; Panyukov, S. *Macromolecules* **1997**, *30*, 8036.
(40) Higgins, J. S.; Benoît, H. C. *Polymer and Neutron Scattering*; Clarendon Press: Oxford, U.K., 1994.
(41) Read, D. J. *Macromolecules* **2004**, *37*, 5065.

MA052357Z